Predicting Turbulent Vertical Velocity in the Ocean Surface Layer under Mixed Convective and Wind/Wave Forcing

ANN. E. GARGETT[a,b]

[a] *Institute of Ocean Sciences, Sidney, British Columbia, Canada*
[b] *Old Dominion University, Norfolk, Virginia*

ABSTRACT: Turbulence in the ocean surface layer is forced by a mixture of buoyancy, wind, and wave processes that evolves over time scales from the diurnal scale of buoyancy forcing, through storm time scales, to the annual cycle. This study seeks a predictor for root-mean-square w (rmsw), a time and surface layer average of turbulent vertical velocity w measured by bottom-mounted vertical-beam acoustic Doppler current profilers, in terms of concurrently measured surface forcing fields. Data used are from two coastal sites, one shallow (LEO, 15-m depth) and one deeper (R2, 26-m depth). The analysis demonstrates that it is possible to predict observed rmsw with a simple linear combination of two scale velocities, one the convective scale velocity w_* familiar from the atmospheric literature, the other a scale velocity w_S representing combined wind and wave effects. Three variants are considered for this latter scale velocity, the wind stress velocity u_* alone and two forms using both u_* and U_S, a Stokes velocity characteristic of the surface wave field. At both sites, the two-parameter fit using u_* alone is least accurate, while fits using the other two variants are essentially indistinguishable. At both sites, the coefficient multiplying w_* is the same, within error bounds, and within the range of previous observations. At the deeper site, the coefficient multiplying the wind/wave scale velocity w_S is approximately half that at the shallow site, a difference here attributed to difference in wave character.

KEYWORDS: Atmosphere-ocean interaction; Langmuir circulation; Oceanic mixed layer

1. Introduction

Turbulence in the surface layer of the open ocean is forced by continuously changing conditions of surface buoyancy flux B_o and wind stress τ. Surface buoyancy forcing usually has strong diurnal variation: buoyancy flux that is stabilizing to the ocean during daylight hours is replaced by destabilizing convective forcing overnight. This basic diurnal cycle can also be modulated on longer time scales, associated with passage of weather systems, that are characteristic of wind stress forcing that drives both mean currents and waves. The challenge addressed here is prediction of the magnitude of mixed layer averaged root-mean-square turbulent vertical velocity rmsw as a function of mixed convective and wind/wave surface forcing conditions. Apart from its role as a key metric for the strength of turbulent motions in the ocean surface layer (OSL), the magnitude of rmsw is a major determinant of the vertical transport of particles such as bubbles, detritus, and plankton. Since such particles affect processes as diverse as air–sea transfers of major gases, phytoplankton productivity, and the export of particulate organic material from the near-surface ocean, a robust predictor of rmsw would have broad application.

Much of our present understanding of OSL turbulence forced by wind and waves is based on computer simulations using large-eddy simulation (LES) techniques. McWilliams et al. (1997) coined the term Langmuir turbulence (LT) to describe turbulence produced by coupled wind/wave forcing, in which vertical vorticity associated with a stress-driven boundary layer is rotated to horizontal by the Stokes drift associated with the surface wave field. This literature, now massive [Li et al. (2004), Tejada-Martínez and Grosch (2007), and Kukulka et al. (2009) are but a few examples], has provided two somewhat different predictions for vertical velocity and vertical length scales characteristic of LT in a well-mixed OSL of depth H. In an initial LES study of an unstratified water column, Polton and Belcher (2007) concluded that the vertical length scale of LT was the mixed layer depth H, provided H was smaller than the Ekman depth $\delta_{\mathrm{Ek}} = u_*/f$. A subsequent study (Grant and Belcher 2009) found that the turbulent vertical velocity scaled as $w_{*L} = (u_*^2 U_{S0})^{1/3}$ where U_{S0} is the surface Stokes drift velocity. A second set of LES led Harcourt and D'Asaro (2008) to conclude that the vertical depth scale of LT was influenced by the e-folding depth of the surface wave field, and that the vertical velocity scale for eddies of $O(H)$ in the LT limit was described by the form proposed by Grant and Belcher (2009), but computed using a surface-layer Stokes velocity, defined as $U_{\mathrm{SL}} = \langle u^S \rangle_{\mathrm{SL}} - u_{\mathrm{ref}}^S$, in place of U_{S0}. Here $\langle u^S \rangle_{\mathrm{SL}}$ is the vertical average of the Stokes velocity from a depth of $0.2H$ to the surface and u_{ref}^S is a deep reference Stokes velocity evaluated near H.

Two fundamental issues arise with use of the results of many LES studies focused on LT in the OSL. The first issue is just that focus, i.e., many studies focus on LT alone, regardless of the presence of buoyancy forcing of either sign (e.g., Sullivan et al. 2004; Noh et al. 2004; Harcourt and D'Asaro 2008; Grant and Belcher 2009; Kukulka and Harcourt 2017). The second is that many LES studies of LT over the past two decades report results at steady state, after a minimum of one (McWilliams et al. 1997) to several (Yan et al. 2022) inertial periods, a time extent between ~1 and several days at midlatitudes. In the actual OSL, steady state over such extended periods is an

Corresponding author: Ann E. Gargett, gargettann@gmail.com

exception rather than the rule, if for no other reason than the diurnal cycle of the buoyancy forcing that is inevitably present to some extent in conjunction with wind/wave forcing. While some LES studies include mixed, non-steady-state forcing (e.g., Skyllingstad and Denbo 1995; Sullivan et al. 2012; Li et al. 2013), the specific question of predicting OSL rmsw over a typical range of time-varying, mixed surface forcings has not been a focus: it thus seems appropriate to examine direct observational evidence that can be brought to bear on this question.

2. Available data and assumed functional form

A preliminary attempt to derive a predictor for rmsw was made by Gargett (2022, hereafter G22), using direct observations of vertical velocity w from the vertical acoustic beam of a vertical-beam ADCP (VADCP) deployed on a bottom node of the Long-Term Ecological Observatory (LEO) coastal observatory, located ~6 km off the shore of New Jersey in water of depth $H = 15$ m, and cabled directly to shore. That analysis involved various assumptions that are either further explored or replaced in this expanded treatment. Specifically, the question of how best to calculate a characteristic (near) surface Stokes velocity for use in various proposed wind/wave scale velocities is explored in section 3, while the assumption made by G22 that extreme locations in forcing space represent "pure" cases dominated by either convection or wind/wave (Langmuir) forcing is removed. The present analysis also expands to include similar direct observations of w from a coastal location much farther from shore (Savidge and Gargett 2017), where a VADCP was deployed on a node cabled to a naval tower (R2) located ~65 km off the coast of Georgia in water of depth $H = 26$ m: data were returned to shore by microwave link. At both locations, time-continuous data from a session (typically 4 days at LEO and 7 days at R2) are divided into sequential 2-h records.

Turbulent vertical velocity w is extracted by first low-pass filtering total vertical beam velocity to remove velocities associated with the passage of surface waves (spatial scales remaining after this filtering are much larger than horizontal diameters of the vertical beam spreads at the surface, 0.7 m at LEO and 1.7 m at R2), then removing a time-local (~2 h) mean from each bin of velocity data. An observational value of wvar $\equiv \overline{\langle w^2 \rangle}$ is computed as w^2 averaged over the time (~2 h) of a standard record length (angle brackets) and over depth (overbar: because the vertical beam measurement is unaffected by sidelobes, the depth average is to the minimum value over the record length of the surface as identified in vertical beam backscatter amplitude). Correction for observational noise variance w_n^2 [1] determines the value used for rmsw as rmsw $\equiv \sqrt{\text{wvar}} = \sqrt{\overline{\langle w^2 \rangle} - w_n^2}$. As defined, rmsw becomes zero when $\overline{\langle w^2 \rangle}$ falls to its noise level.

Associated surface forcings are derived from direct tower-based observations of wind speed and of the terms involved in estimating surface buoyancy flux B_o (defined as positive when destabilizing to the ocean) from net heat flux Q. Full descriptions of the observational sites, derivation of τ and B_o, Doppler instruments and their deployments, the vertical beam measurement of vertical velocity and its subsequent processing are found in Gargett and Wells (2007) for LEO and Savidge and Gargett (2017) for R2.

Data used from both locations have two major qualifications. First is restriction to times when the water column is "unstratified" over water column depth H. Since salinity is not available at either location, stratification $\Delta\rho/\Delta z \sim \alpha\Delta T/H$ is defined in terms of ΔT, the change in temperature over H, available at both sites from nearby thermistor chain moorings. The value of $\Delta T < 0.5°\text{C}$ used to define "unstratified" at LEO is essentially the same at R2, due to nearly compensating changes in H and α. Second, although not a problem with the weak tides typical of LEO, stronger tides at R2 raise the possibility of contamination from periods of low convective and wind/wave forcing but maximum tidal flows, periods characterized by a near-bottom maximum in rmsw. Thus, a second major qualification is that the record(time)-averaged profile of rmsw must have its maximum in the upper half of the water column.

Some assumptions are made in the following analysis. First it is assumed that the dominant waves are aligned with the wind. Although various LES studies have found significant effects of nonalignment (e.g., Van Roekel et al. 2012), observational studies (D'Asaro et al. 2014, online supplemental material; Wang et al. 2022, their Fig. 4a) indicate a strong tendency for wind-driven waves to be at least approximately wind aligned. Given these results, plus a recent conclusion by Fan et al. (2020) that LES solutions in cases with large wind/wave misalignment are sensitive to the subgrid models used and need to be considered with caution, the simplifying assumption of wind-aligned waves is reasonable for an exploration of combined surface forcings. This is particularly the case if, as argued by Csanady (1994), Teixeira and Belcher (2002), and Sullivan et al. (2007), wave *breaking* supplies a major source of seed vorticity for the Craik–Leibovich (CL2; Leibovich 1983) instability that generates Langmuir circulations (LC), since wave breaking occurs primarily in the downwind direction. Another underlying assumption made here is that in the real world there is only rarely a case of pure wind forcing, if that is defined as wind forcing that results *only* in a classical stress-driven boundary layer. Imposition of wind stress τ on the ocean surface is accompanied by surface wave generation, hence the presence of forces generating Langmuir circulations in addition to mean flow. Exceptions to this co-occurrence are conditions of short fetch, such as those reported in Wang et al. (2022) and G22 or rapidly changing wind direction (Gargett and Savidge 2020; Wang and Kukulka 2021).

Given these assumptions, the hypothesis explored is that the observed (noise-corrected) value of rmsw in cases of mixed wind/wave and destabilizing buoyancy forcing can be predicted by the weighted sum of one scale velocity w_* characteristic of convection and a second scale velocity w_S

---

[1] Noise variance w_n^2 is estimated as a typical minimum (nearest-bottom) observed value of record (time)-averaged $\langle w^2 \rangle$: for profile examples, see Gargett and Wells (2007, their Fig.8). $w_n^2 = 9 \times 10^{-5} (\text{m s}^{-1})^2$ for LEO; $w_n^2 = 1.7 \times 10^{-4} (\text{m s}^{-1})^2$ for R2. Only a few values of $\langle w^2 \rangle < w_n^2$ appear in each dataset (and are not used in this analysis), suggesting that the values chosen for w_n are appropriate.

characteristic of combined wind/wave forcing. The hypothesized relationship is

$$\text{rmsw} = a_o + a_C w_* + a_S w_S, \qquad (1)$$

where an offset a_o, assumed negative and small, allows for the fact that removal of a noise level from the observed value of $w$var during processing will have resulted in an observed value of rmsw that is somewhat smaller than the full predicted value of $a_C w_* + a_S w_S$. The simple linear combination of Eq. (1) has the basic property of approaching one end member when the other becomes small.

A convective scale velocity $w_* \equiv (B_o H)^{1/3}$, where $B_o > 0$ is buoyancy flux from the ocean to the atmosphere and H is mixed layer depth, has a long history from the convective atmospheric boundary layer (Holtslag and Nieuwstadt 1986). Here $B_o = (g\alpha Q/\rho_o C_v)$ is calculated from observed total heat flux Q using $g = 9.81$ m s^{-2} and reference seawater density $\rho_o = 1024$ kg m^{-3}. Values of C_v, the specific heat of seawater at constant volume, and α, the thermal expansion coefficient of seawater, are those appropriate to average ocean surface temperatures of 10°C at LEO ($C_v = 4.19 \times 10^3$ J kg^{-1} K^{-1}, $\alpha = 1.7 \times 10^{-4}$ K^{-1}) and 25°C at R2 ($C_v = 4.00 \times 10^3$ J kg^{-1} K^{-1}, $\alpha = 2.98 \times 10^{-4}$ K^{-1}). The term H is water column depth, since only unstratified records are analyzed.

In contrast to the well-defined and tested convective scale velocity, the oceanographic literature contains various suggestions for a wind/wave scale velocity. Here I consider three frequently proposed candidates:

$$w_{S1} = u_* = \sqrt{\tau/\rho_o}, \qquad (2a)$$

where ρ_o is a reference density of seawater, as used by D'Asaro (2001) and Tseng and D'Asaro (2004),

$$w_{S2} = (u_* U_S)^{1/2}, \qquad (2b)$$

as defined by Leibovich (1983) and simplified by Plueddemann et al. (1996), and

$$w_{S3} = (u_*^2 U_S)^{1/3}, \qquad (2c)$$

originally defined by Smith (1996) as a scale for horizontal motions of LT, but derived by subsequent authors (Harcourt and D'Asaro 2008; Belcher et al. 2012) as a scale for vertical motions.

In Eqs. (2b) and (2c), U_S is a characteristic Stokes velocity. While this has most frequently been taken as the surface value, it is desirable to determine a "best" value to use for U_S in (2b) and (2c) before proceeding to examine their use in Eq. (1).

3. Determination of a best value for U_S

In this section, I consider three possible choices (among many) for U_S. All three are calculated in different ways from a spectral Stokes function derived [after Kenyon (1969), assuming wind-aligned waves] from a surface wave displacement spectrum $\phi_s(\omega)$. Using a vertical coordinate x_3, which is

zero at the mean sea surface and increases upward, the Stokes velocity at depth $x_3 < 0$ below the surface is taken as

$$U_S(x_3) = \int_0^{\omega_B} \phi_s(\omega)\omega k \frac{\cosh 2k(x_3 + H)}{\sinh^2 kH} d\omega, \qquad (3)$$

where the upper limit of integration ω_B is a wave breaking frequency defined by the work of Forristall (1981), taken by Clarke and Van Gorder (2018) as the maximum frequency at which motions may be considered as irrotational waves. The surface wave displacement spectrum used here is calculated from vertical velocity measured as close as possible to the surface, as described and validated in the appendix of Gargett and Grosch (2014, hereafter GG14).

The three possibilities considered for U_S are

1) the surface value

$$U_{S0} = U_S(x_3 = 0);$$

2) the value of U_S at a fixed depth below the surface, here taken as

$$U_{S3} = U_S(x_3 = -3\text{ m}); \quad \text{and}$$

3) a near-surface-integral Stokes drift velocity defined as

$$\text{int}U_{S3} = \frac{1}{3\text{m}} \int_{x_3 = -3\text{m}}^{0} U_S(x_3) dx_3,$$

the integral of the Stokes drift velocity from $x_3 = -3$ m to the surface.

The depth of 3 m is chosen in (2) and (3) primarily because that is the depth at which GG14 found that the Stokes shear critical to LC generation becomes bounded within the range of measured frequency at LEO, hence completely determined by the observations [note that for typical wave fields, the Kenyon (1969) form produces infinite Stokes shear at the surface, as a result of contributions from small-wavelength, high-frequency waves: see discussion in appendix of GG14]. GG14 used Stokes *shear* at 3-m depth in calculating a value for Leibovich's (1977) growth rate for Langmuir circulations, subsequently used by G22 to define a forcing space that allows qualitative determination of the mixture of convective and wind/wave forced turbulence from associated surface forcing. The depth of 3 m is also shallow enough that this value of Stokes drift velocity can be considered a characteristic near-surface value, without the disadvantages of U_{S0} that will be examined below. While using 3-m depth here retains continuity with previous published results, another near-surface depth could be used without difference in outcome, save for the value of the constant a_S.

Figure 1 cartoons the behavior of the above 3 possibilities for waves of wavelength long (Fig. 1a) and short (Fig. 1b) compared with the depth of 3 m.

While the surface value U_{S0} has been most widely used as a characteristic Stokes velocity in LES, it has issues that make it less than ideal for use with observations. Foremost is the
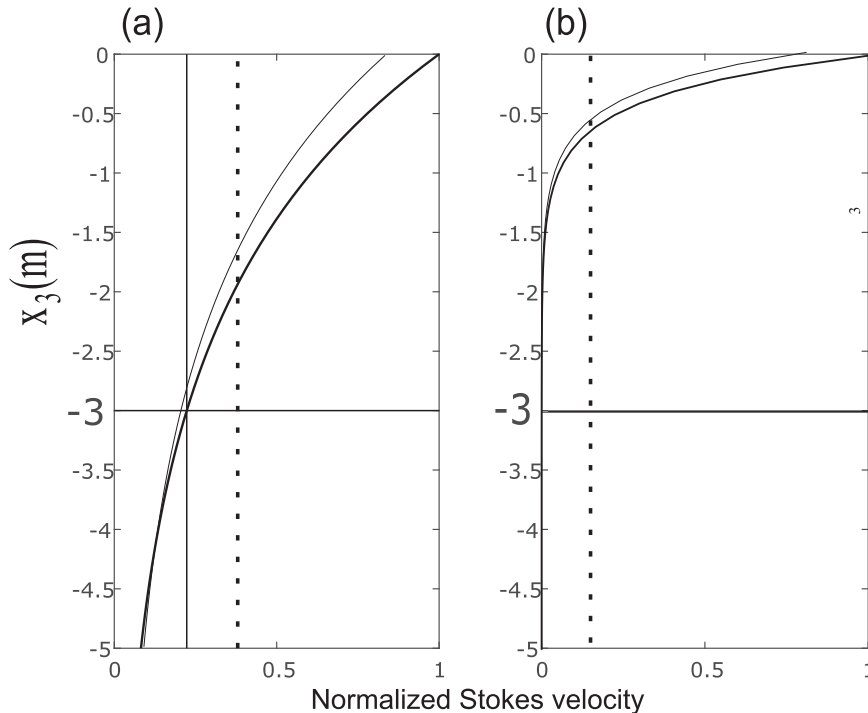
FIG. 1. Cartooned profiles of measured Stokes velocity (U_S^M, light solid curve), and Stokes velocity corrected for missing variance at frequencies higher than the upper limit of measurements (U_S, heavy solid curve), normalized to 1 at the surface value $U_{S0} = U_S (x_3 = 0)$, for cases of dominant waves of length (a) long and (b) short compared to the depth of 3 m. Associated values of $U_{S3} = U_S (x_3 = -3$ m$)$ (solid vertical line) and intU_{S3}, defined as the integral of U_S from $x_3 = -3$ m to the surface (dotted vertical line) are also cartooned for each case. In (b), U_{S3} is assumed effectively coincident with the vertical axis.

necessity of correcting U_{S0}^M, the value derived from surface wave displacement spectra measured to some upper frequency f_M (usually of order 0.5 Hz), for variance due to missing higher-frequency waves in order to produce a value for U_{S0}. This correction has been done in various ways, all based on (different) assumed spectral forms of wind-forced waves (e.g., Belcher et al. 2012; Clarke and Van Gorder 2018): the corrected values shown in Fig. 2a use the correction method described in the appendix of G22. While each method that has been defined produces a slightly different result, a more serious concern is the lack of an accepted correction technique when waves are determined *not* to be actively wind-forced
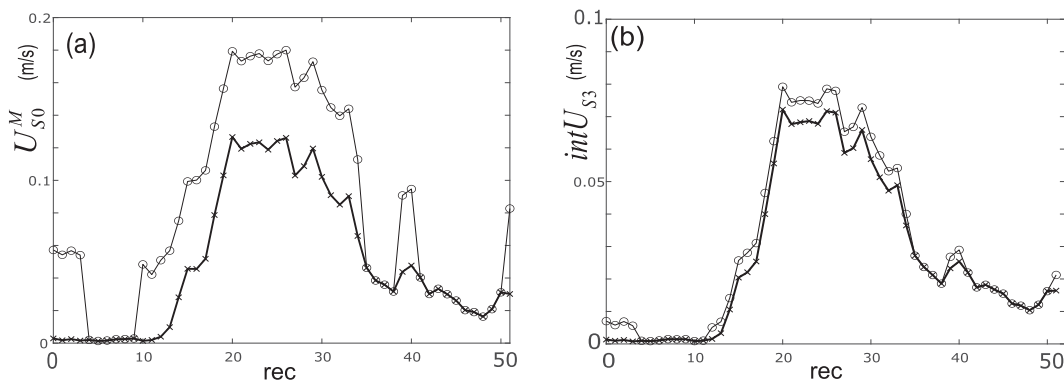

FIG. 2. Values of (a) U_{S0} and (b) intU_{S3} as functions of record number for LEO session 043. In both panels, the heavy line shows values originally derived from surface wave displacement spectra measured to an upper frequency $f_M = 0.4$ Hz, and the light line shows those values corrected for missing variance at frequencies $f_M < f < f_B$, where f_B is the wave breaking frequency of Forristall (1981). Periods where corrected and uncorrected curves coincide are those when the surface wave field is determined (by the ECMWF criterion) to be *not* wind forced.

TABLE 1. LEO values of the coefficients in Eq. (1), with error bounds in square brackets, as determined from a fit to observed values of rmsw using the two parameters w_* and w_{Si} calculated from observed surface forcing fields. Here $w_{S1} = u_*$, $w_{S2} = (u_* U_S)^{1/2}$, and $w_{S3} = (u_*^2 U_S)^{1/3}$, the latter two calculated with the near-surface-integral value $U_S = \mathrm{int}U_{S3}$. Entries in parentheses () are results of fits using w_{S2} and w_{S3} calculated with $U_S = U_{SL} = \mathrm{int}U_{S3} - u_{\mathrm{ref}}^S$, the surface-layer value at LEO.

$N = 149$	w_{S1}	w_{S2}	w_{S3}
a_o	0.0002 [−0.0014, 0.0017]	−0.0017 [−0.0029, −0.0005] (−0.0014 [−0.0026, −0.0002])	−0.0014 [−0.0026, 0.0002] (−0.0012 [−0.0023, 0.0000])
a_C	0.166 [0.019, 0.312]	0.544 [0.429, 0.658] (0.517 [0.406, 0.629])	0.452 [0.339, 0.565] (0.431 [0.319, 0.5423])
a_S	1.51 [1.39, 1.62]	0.577 [0.544, 0.610] (0.600 [0.566, 0.634])	0.812 [0.766, 0.858] (0.830 [0.783, 0.877])
rmse (m s^{-1})^2	0.002 13	0.001 64 (0.001 60)	0.001 62 (0.001 61)
R^2	0.815	0.891 (0.896)	0.893 (0.895)

waves [using the ECMWF criterion (Bidlot 2020), as discussed in G22]. Such situations, which include those of swell domination and/or decaying wind waves, are not uncommon in measurements. There is no present basis for correction of such records, leading to the discontinuities in U_{S0} seen in Fig. 2a.

A final problem with determining U_{S0} occurs in cases where the peak of the Stokes spectrum lies at frequencies very near or beyond the maximum observed frequency f_M: in such cases U_{S0} is indeterminate.

Because Stokes velocities associated with high-frequency waves drop off rapidly with depth, correction for missing high-frequency variance is much smaller in U_{S3} (not shown), than in U_{S0}: hence in this regard U_{S3} is preferable to U_{S0}. However, as cartooned in Fig. 1b, U_{S3} can fall to near zero while finite Stokes drift velocities due to high-frequency, short-wavelength waves remain at shallower depths. The best characteristic Stokes velocity would seem to be one that retains a nonzero (even if small) value under these conditions, but remains relatively unaffected by a missing variance correction.

The third form above fulfills both of these conditions. The missing variance correction for wind-forced waves in $\mathrm{int}U_{S3}$ (see the appendix) is much smaller than that in U_{S0} and as a result, discontinuities in $\mathrm{int}U_{S3}$ across wind-forced/not-wind-forced wave boundaries are much less severe, as seen in Fig. 2b. As well, the value of $\mathrm{int}U_{S3}$ remains finite in cases dominated by high-frequency waves. Thus, for use in the scaling velocity forms (2b) and (2c), I will use $U_S = \mathrm{int}U_{S3}$ as the best estimate of a characteristic near-surface Stokes velocity. Note that $x_3 = -3$ m $= -0.2H_{\mathrm{LEO}}$ at LEO, hence this near-surface-integral value, when corrected for near-bottom Stokes drift, equals the surface-layer value suggested by the LES analysis of Harcourt and D'Asaro (2008). For R2, $\mathrm{int}U_{S3}$ remains the near-surface-integral value, while the surface-layer value is $\mathrm{int}U_{S5} - u_{\mathrm{ref}}^S$, defined as the integral from $x_3 = -5.2$ m $= -0.2H_{R2}$ to the surface, corrected for bottom Stokes drift. This surface-layer value is also computed for the R2 data and will be assessed relative to $\mathrm{int}U_{S3}$ in section 5.

4. Scaling rmsw at LEO

Testing Eq. (1) requires determination of the constants a_C and a_S that multiply respectively convective and wind/wave scale velocities. To determine these constants, all qualified data are used in MATLAB fits using two variables, the convective scale velocity w_* and one of the three expressions (2a), (2b), or (2c) for w_S. Records are considered qualified if they fulfill the following conditions:

- the Stokes spectrum peaks below the maximum observed frequency f_M;
- the water column is unstratified;
- surface buoyancy forcing is convective, i.e., $B_o > 0$;
- $\overline{\langle w^2 \rangle} > w_n^2$; and
- the record(time)-averaged profile of rmsw has its maximum in the upper half of the water column.

Note that this procedure for determining a_C and a_S, unlike that of G22, makes no assumptions about particular records being pure convection or pure LC. It is expected that the coefficient fit for a_C will be constant across the three fits involving the three different versions of U_S, while the coefficient a_S will depend on the assumed form of U_S.

For all three fits to the LEO data, residuals approach normality (hence error bounds are reliable) and coefficients approach approximately constant values when the number of records $N > \sim 100$, more than fulfilled by the set of $N = 149$ qualified records.

For the LEO dataset, Table 1 shows fit parameters with error bounds in square brackets for each of the three candidates for characteristic wind/wave velocity, calculating both $w_{S2} = (u_* U_S)^{1/2}$ and $w_{S3} = (u_*^2 U_S)^{1/3}$ with $U_S = \mathrm{int}U_{S3}$. Also shown for each are values of root-mean-square error rmse $= \mathrm{sqrt}\left[\sum_{i=1}^N (\mathrm{rmsw} - \mathrm{rmsw}^{\mathrm{fit}})^2/(N-3)\right]$, where rmsw and rmsw$^{\mathrm{fit}}$ are observed and fitted values, respectively, as well as the R^2 value of the fit. In Table 1, parameters in parentheses for w_{S2} and w_{S3} result from separate fits using the surface-layer value $U_{SL} = \mathrm{int}U_{S3} - u_{\mathrm{ref}}^S$, where u_{ref}^S is taken as the Stokes drift velocity calculated at $x_3 = -H$ (using the value at $x_3 = -0.8H$ (not shown) makes no noticeable difference to the results), in place of the near-surface integral value $\mathrm{int}U_{S3}$. Figures 3a–c show scatterplots of observed values of rmsw and residuals (rmsw–rmsw$^{\mathrm{fit}}$) versus rmsw$^{\mathrm{fit}}$ for all records used in the fits. Figure 3d shows the same for the fit using the surface-layer value to calculate w_{S2}.

Table 1 shows that the fit associated with w_{S1} has the largest value of rmse and smallest value of R^2 of the three, suggesting
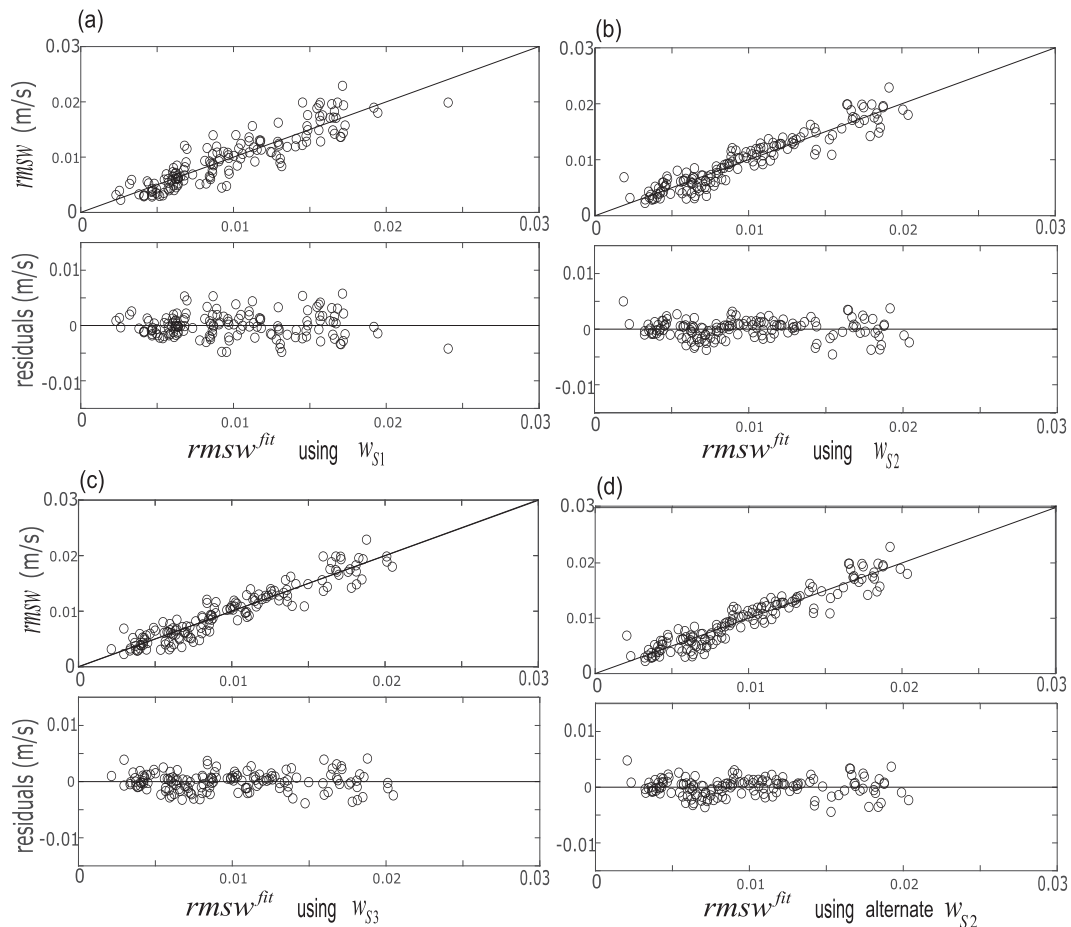
FIG. 3. The upper panels in each group show values of rmsw observed at LEO as a function of values predicted using observational values of w_* and either (a) $w_{S1} = u_*$, (b) $w_{S2} = (u_* U_S)^{1/2}$, or (c) $w_{S3} = (u_*^2 U_S)^{1/3}$, with the latter two calculated using the near-surface-integral value $U_S = \text{int}U_{S3}$. The solid line is a 1/1 relationship, a line with slope 1 through the origin. The lower panels in each group show the associated residuals (rmsw − rmsw$^{\text{fit}}$). (d) For comparison with (c), results for the alternate fit using w_{S2} calculated with the LEO surface-layer value of $U_S = U_{\text{SL}} = \text{int}U_{S3} - u_{\text{ref}}^s$.

that it is indeed useful to add information about wind/wave forcing via use of a Stokes drift velocity in either w_{S2} or w_{S3}. Thus, first restricting comments to features of these latter two choices:

1) For both fits, the offset a_o is approximately the same magnitude and negative, consistent with the fact that the observations being fitted are corrected by subtraction of a noise level, so the prediction of total rmsw by $a_C w_* + a_S w_S$ should be decreased by some (small) amount.

2) The convective scale velocity coefficient a_C is the same, within error bounds, for both fits, consistent with expectation that the convective and wind/wave scale velocities are independent, provided they are chosen properly.

3) The fits using w_{S2} and w_{S3} are associated with only minor difference in goodness of fit parameters. This feature would result if $U_S \propto u_*$, i.e., if the characteristic Stokes velocity were nearly linearly proportional to the surface stress velocity. However, the proportionality cannot be

exact, or else the stress velocity itself would work equally well as a wind/wave scaling velocity, which is not the case.

4) There is very little change in either the a_S coefficient or goodness of fit parameters when $U_S = \text{int}U_{S3} - u_{\text{ref}}^S$ is used in place of $U_S = \text{int}U_{S3}$ when calculating w_{S2} or w_{S3}.

In contrast to (2) above, when using $w_{S1} = u_*$ as the wind/wave scale velocity, the fit coefficient a_C obtained for the convective scale velocity is significantly different from the average value of a_C obtained using w_{S2} and w_{S3}. Moreover the offset a_o has positive rather than the expected negative sign. These features, plus decreased goodness of fit and increased rmse, indicate that among those considered, u_* is the least desirable choice for a wind/wave scaling velocity at this site.

5. Scaling rmsw at R2

I now turn to the question of whether the constants that characterize Eq. (1) at LEO are the same as those determined

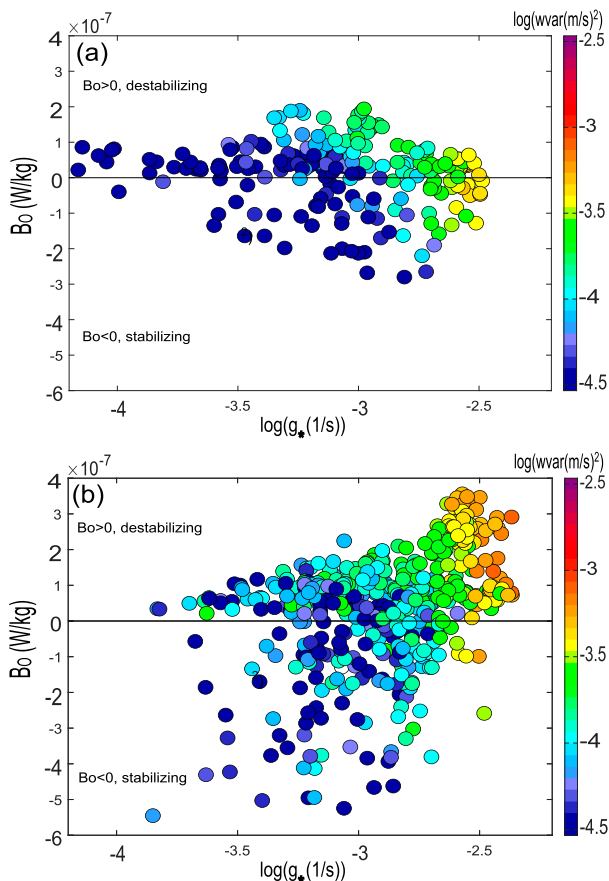FIG. 4. All qualified records, color coded by magnitude of wvar, from (a) LEO and (b) R2 are shown in the forcing space of near-surface Langmuir circulation growth rate calculated as $g_* \equiv [(dU_S/dx_3)_{x_3=-3m}(u_*/H)]^{1/2}$ and surface buoyancy flux B_o, as defined by G22. Using $\log(g_*)$ expands resolution of low values of g_*: similarly, color coding $\log(wvar)$ reveals increased detail of signal strength.

with a similar dataset from R2, the location in deeper water, farther from shore. First, it is useful to consider similarities/differences of the two datasets in the forcing space defined by G22, using surface buoyancy flux B_o and the growth rate

$g_* = [(dU_S/dx_3)(dU/dx_3)]^{1/2}$, evaluated near the surface, that Leibovich (1977) demonstrated is a characteristic growth rate for Langmuir circulations. Following GG14, g_* is evaluated using Stokes shear at $x_3 = -3$ m and approximating mean shear as u_*/H. G22 demonstrates the connection between location in the upper half of this space and the dominance of either buoyancy (moderate B_o, small g_*) or wind/wave (small to moderate B_o, large g_*) forcing of surface layer turbulent structures. Distributions of data in this space are seen in Fig. 4 for both LEO and R2: both signs of surface buoyancy forcing are shown, although here the focus is on convective records with $B_o > 0$.

As seen in Fig. 4, overall magnitudes of wvar = rmsw^2 are similar in the regions where the distributions overlap. However, there are significant differences. The R2 dataset, despite being larger than that from LEO, has no situations with very low g_*. This is consistent with the fact that the few measurements of very low g_* at LEO were associated with a rare condition of weak winds with very short offshore fetch. While R2 has some records with slightly higher g_* than LEO, the most noticeable difference is the presence of records with much higher buoyancy flux at large values of g_*, filling in one of the "holes" pointed out in G22. These larger buoyancy fluxes are associated with the higher surface layer temperature at R2. Finally, R2 also has many more records with large *stratifying* buoyancy flux, although these aren't considered in the present analysis.

For a set of R2 data qualified by the same criteria as those for LEO, residuals approach normality (hence error bounds are reliable) and coefficients approach approximately constant values when the number of records $N > \sim 200$ (the fact that this number is larger than that determined for LEO is likely associated with larger scatter of observed rmsw at R2 relative to LEO, discussed further below). The $N = 288$ qualified R2 records are adequate to determine stable coefficients.

Carrying out the procedure outlined in section 4 on qualified R2 data using the near-surface-integral value $U_S = \text{int}U_{S3}$ in calculation of w_{S2} and w_{S3} results in the fits shown on the upper lines of Table 2, while results using the surface-layer value $U_{SL} = \text{int}U_{S5} - u_{\text{ref}}^S$ are shown in brackets on the lower lines. Figure 5 shows the same fits seen in Fig. 3 for LEO.

At R2, the fit using u_* again has the largest value of rmse and smallest value of R^2, although the differences are smaller

TABLE 2. Values of the coefficients in Eq. (1), with error bounds in square brackets, as determined from a linear fit to values of rmsw observed at R2 using the two parameters w_* and w_{Si} determined from observed surface forcing fields. Here, $w_{S1} = u_*$, $w_{S2} = (u_* U_S)^{1/2}$ and $w_{S3} = (u_*^2 U_S)^{1/3}$, the latter two calculated with the near-surface-integral value $U_S = \text{int}U_{S3}$. Entries in parentheses () are results of fits using w_{S2} and w_{S3} calculated with $U_S = U_{SL} = \text{int}U_{S3} - u_{\text{ref}}^S$, the surface-layer value at R2.

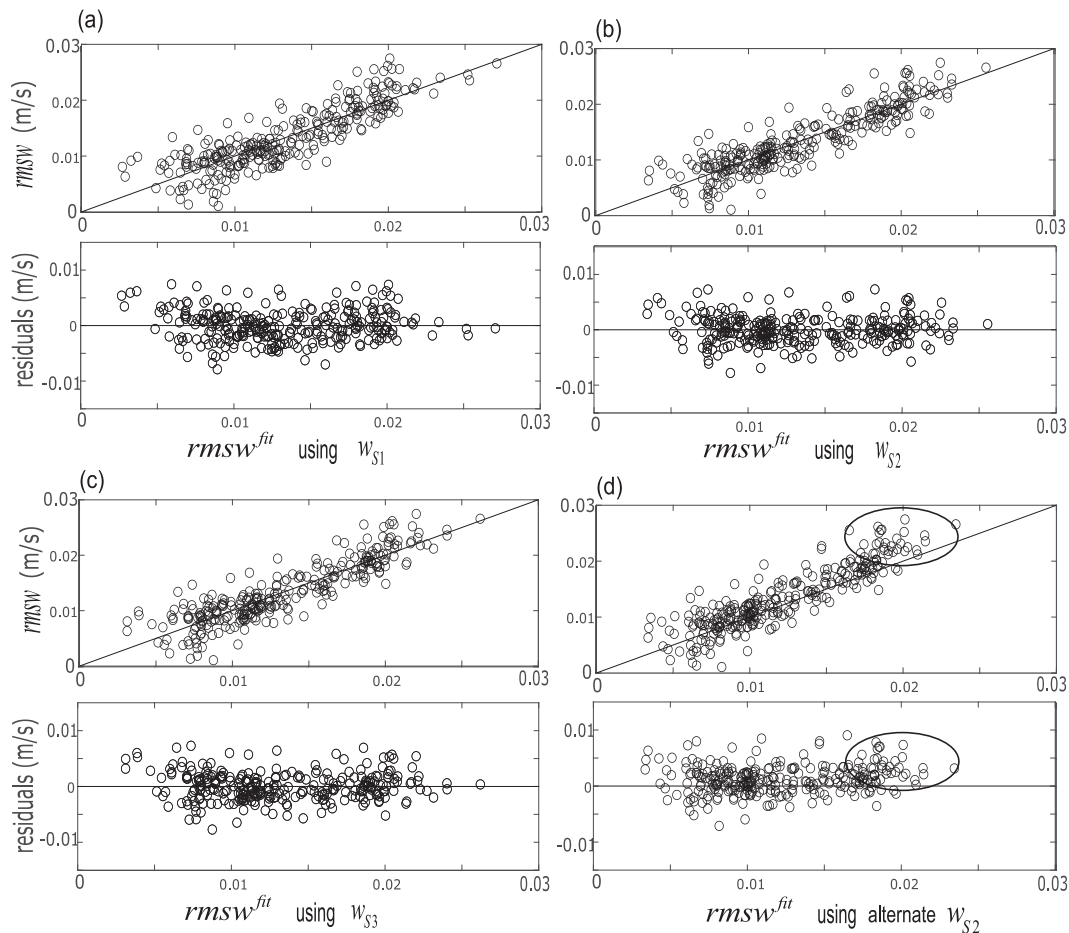| $N = 288$	w_{S1}	w_{S2}	w_{S3}
a_o	-0.0032 $[-0.0047, 0.0016]$	-0.0029 $[-0.0043, 0.0015]$	-0.0030 $[-0.0044, -0.0016]$
		$(-0.0026$ $[-0.0040, -0.0012])$	$(-0.0027$ $[-0.0041, -0.0014])$
a_C	0.488 $[0.373, 0.604]$	0.586 $[0.487, 0.685]$	0.543 $[0.442, 0.644]$
		$(0.587$ $[0.489, 0.685])$	$(0.543$ $[0.443, 0.643])$
a_S	0.735 $[0.666, 0.803]$	0.309 $[0.284, 0.333]$	0.422 $[0.389, 0.455]$
		$(0.353$ $[0.326, 0.380])$	$(0.462$ $[0.426, 0.498])$
rmse $(\text{m s}^{-1})^2$	0.00284	0.00253	0.00255
		(0.00250)	(0.00252)
R^2	0.737	0.792	0.789
		(0.796)	(0.793)

FIG. 5. The upper panels in each group show values of rmsw observed at R2 as a function of values predicted using observational values of w_* and either (a) $w_{S1} = u_*$, (b) $w_{S2} = (u_* U_S)^{1/2}$, or (c) $w_{S3} = (u_*^2 U_S)^{1/3}$, with the latter two calculated using the near-surface-integral value $U_S = \mathrm{int}U_{S3}$ in Eq. (1). The solid line is a 1/1 relationship, a line with slope 1 through the origin. The lower panels in each group show associated residuals (rmsw − rmsw$^{\mathrm{fit}}$). (d) For comparison with (c), results for an alternate fit using w_{S2} calculated with the R2 surface-layer value $U_S = U_L = \mathrm{int}U_{S5} - u_S^{\mathrm{ref}}$. Ellipses highlight a region of consistent underestimation of rmsw by this alternate fit.

in magnitude than those at LEO. Unlike LEO, all 3 fits now have comparable (small, negative) values of a_o and equal (within error bounds) values of a_C, i.e., the major differences in these two coefficients in the LEO fit using $w_{S1} = u_*$ have disappeared. There are, however, additional major differences from LEO. First, as seen in the plots of Fig. 5, the scatter for all of the R2 fits is nearly twice that at LEO, hence values of R^2 are smaller. Second, the wind/wave coefficients determined from the fits using w_{S2} and w_{S3} are both roughly half the comparable values at LEO.

Before discussing these features, it is first necessary to emphasize that they do not result from the choice of $U_S = \mathrm{int}U_{S3}$ for calculation of the scale velocities w_{S2} and w_{S3}. For LEO, Table 1 showed the coefficients resulting from use of $\mathrm{int}U_{S3}$ (upper values) and $\mathrm{int}U_{S3} - u_{\mathrm{ref}}^S$ (lower values, in brackets) in calculation of both w_{S2} and w_{S3}. Within error bounds, there is no significant difference between the two values of a_S because, at LEO, values of u_{ref}^S although increasing with wind

stress, remain a small fraction of $\mathrm{int}U_{S3}$ throughout the range of observed values (see Fig. 7b). Table 2 shows similar coefficients for R2. Here the a_S coefficients obtained using the surface-layer value (i.e., integrating the Stokes velocity from −5.2 m to surface) are only slightly larger than those obtained using the near-surface-integral value, i.e., where the integration is over the same (3 m) layer depth as at LEO (also note that error bounds of the two estimates still overlap). This insensitivity arises partly because $\mathrm{int}U_{S5}$ is only ~20%–30% smaller than $\mathrm{int}U_{S3}$ over the observational range of u_*, plus u_{ref}^S is effectively zero for all conditions at R2 (see Fig. 7a), and partly because w_{S2} and w_{S3} involve respectively the square and cube root of the expression used for U_S. Use of the surface-layer value at R2 does appear to make slight improvement in the reported goodness-of-fit parameters rmse and R^2. However, these parameters are related to the actual fit which, while constrained to be linear, is not constrained to be a 1/1 fit, i.e., a line through zero with slope of 1. Indeed,

the R2 results of Fig. 5d reveal definite underestimation of observed rmsw at large values (ellipses in Fig. 5d), i.e., a departure from a 1/1 fit when using the surface-layer value rather than the near-surface-integral value. This latter result suggests that when computing a characteristic Stokes velocity for use in evaluating wind/wave scaling velocities, a near-surface integral value of Stokes velocity, computed as an integral over a fixed distance from the surface, is preferable to a surface-layer value where integration depth varies with mixed layer depth.

The above results at R2 thus support the conclusion of Grant and Belcher (2009) that the appropriate scale velocity for LT in a well-mixed layer is calculated with a (near) surface value unaffected by mixed layer depth relative to the wavelength of dominant surface waves. The results from both sites indicate that fits using w_{S2} and w_{S3} have nearly identical values of rmse and R^2, hence do not suggest a preference between these two forms as a scale velocity for Langmuir turbulence. Finally, the coefficient values in Tables 1 and 2 show that the observed difference between fitted values of a_S at LEO and R2 is statistically significant.

6. Discussion and conclusions

A final analysis, using fitted data, reinforces a basic premise of the present study, i.e., that a mixture of forcings, rather than pure convective or wind/wave forcing, is more the norm than the exception in the OSL. Figure 6 shows the convective ($B_o > 0$) half-plane of the forcing space defined by G22. Color codes values of $\log(R_F \equiv a_{S2}w_{S2}/a_C w_*)$, where the forcing ratio R_F is the ratio of the vertical velocity of the wind/wave component relative to the convective component, using fits to both LEO and R2 data made with $U_S = \text{int}U_{S3}$ in calculation of w_{S2}.[2] Using the logarithm of R_F results in a $[-1, 1]$ range that covers cases where wind/wave forcing dominates ($\log R_F \gg 0$) and where convection dominates ($\log R_F \ll 0$). The region of white in the middle of the color bar highlights values within ±20% of the value of $R_F = 1$ that corresponds to equal contributions from the two turbulence sources. The shift in the distribution of the ratio toward higher values of $\log(g_*)$ at R2 relative to LEO arises from the difference of approximately a factor of 2 between the values of a_S, hence magnitude of wind/wave forcing, at the two sites as documented in Tables 1 and 2 (a possible explanation for this difference will be discussed below). Despite this difference, in both locations there are clear bands of white-coded records, those in which buoyancy and wind/wave forcings make approximately equal contributions to observed rmsw. These bands trend upward as $\log(g_*)$ increases, i.e., the buoyancy flux required for the convective component to equal the wind/wave component increases with $\log(g_*)$. While there certainly are situations in which wind/wave forcing dominates ($\log > 0.5$ corresponds to wind/wave forcing more than ~3 times convective forcing) and those in which convective forcing dominates ($\log < -0.5$ corresponds to convective forcing more than ~3 times wind/wave
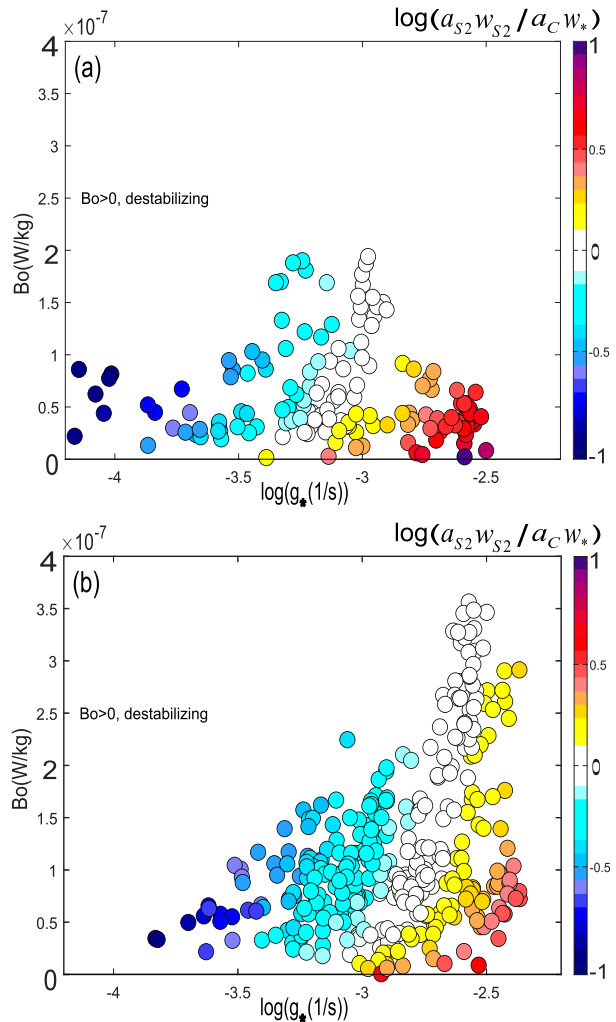

FIG. 6. (a) LEO and (b) R2 data in the upper half of the forcing space of near-surface Langmuir circulation growth rate $g_* \equiv [(dU_S/dx_3)_{x_3=-3\text{m}}(u_*/H)]^{1/2}$ and surface buoyancy flux B_o. Color codes $\log(R_F \equiv a_{S2}w_{S2}/a_C w_*)$, where R_F is the ratio of the contribution to rmsw from wind/wave forcing to that from buoyancy forcing, and the wind/wave scale velocity w_{S2} is calculated using $U_S = \text{int}U_{S3}$.

forcing), the number of records in which the two have comparable magnitudes is striking.

The present demonstration that observed ocean surface layer turbulence frequently results from a mixture of convective and wind/wave forcing is consistent with analysis by Belcher et al. (2012) of ERA reanalysis data of surface forcing in the Southern Ocean in winter. In a space of regime parameters defined by Belcher et al. (2012), the peak of a joint pdf of observations lies midway between regime regions defined as dominated by buoyancy forcing and wind/wave (in present terminology) forcing. The conclusion is also consistent with LES results of Walker et al. (2016), who found that a large heat flux (560 W m^{-2}, corresponding to $B_o \sim 2.2 \times 10^{-7}$ W kg^{-1} at LEO) was required for convection to exceed the (storm force)

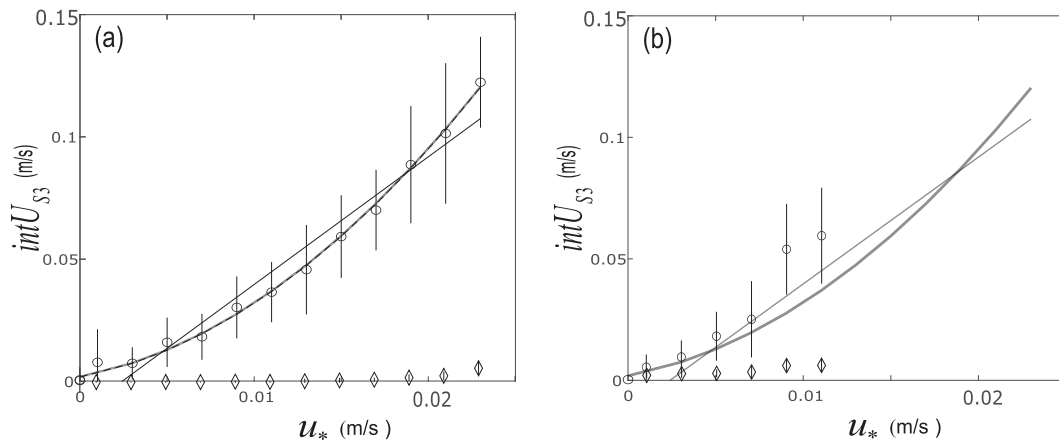[2] While Fig. 6 uses the wind/wave scale velocity w_{S2}, similar plots using w_{S3} (not shown) are essentially identical.

FIG. 7. Relationship between the near-surface-integral Stokes drift velocity intU_3 and u_* for binned records from (a) R2 and (b) LEO. The first-order (thin straight line) and second-order (heavy curve) fits to the R2 data are shown in both panels. Diamonds on each panel are binned values of u_{ref}^S.

wind/wave forcing contribution to computed turbulent kinetic energy. Using parameter values in Walker et al. (2016) and an appropriate single-wave version of the Stokes drift profile, their LES is found to be characterized by a value of $\log(g_*) \sim -2.6$, a value at the high end seen for that parameter at LEO. While none of the direct observations near this value of $\log(g_*)$ have convective fluxes in excess of $\sim 2 \times 10^{-7}$ W kg^{-1}, given the upward slope of the white band in Fig. 7a, it is clear that buoyancy flux in excess of this value would indeed be required for convection to make a contribution to observed rmsw that is comparable to the computational wind/wave contribution.

Having reiterated the necessity of a predictive algorithm for rmsw that incorporates both buoyancy and wind/wave forcing, it is necessary to understand the statistically reliable differences between wind/wave scalings derived for LEO and R2, as well as the increased scatter in the R2 results. For any such understanding, it first needs to be recognized that the physical environment at R2 differs from that at LEO in a number of possibly significant ways.

1) Because R2 is much farther from a coast than LEO, it seemed possible that the horizontal pressure gradient produced by Ekman transport in the presence of a nearby coast, a pressure gradient that rapidly produces steady shore-parallel flow at LEO (Grosch and Gargett 2016), would take longer at R2, implying stronger effects of rotation, disrupting the organized Langmuir cells typical of LEO and producing the less organized, weaker structures characteristic of Langmuir turbulence (McWilliams et al. 1997) at R2. However, examination of mean current hodographs (not shown) reveals that, within uncertainty associated with definition of the "start" of a wind event, mean current response times are $\sim$6–8 h at both locations, removing differences in inertial effects as a major factor in observed differences in turbulence structure and strength.

2) Tidal flows at R2 have typical magnitude of $\sim$0.4 m s^{-1}, much larger than the 0.1 m s^{-1} typical of LEO. Although records that were possibly contaminated by strong tidal

bottom boundary layers were rejected, it is possible that other effects of tides may remain, as will be discussed below.

3) The dominant storm-driven surface waves at R2 are close to deepwater waves (Fig. 14b of Gargett et al. 2014), while those at LEO during strong wind events are of intermediate type (Fig. 14a of Gargett et al. 2014).

4) Observations clearly show that during storms, bottom stress at LEO rises rapidly to equal the applied surface wind stress in magnitude (Gargett and Savidge 2020, their Fig. 12a). In contrast, bottom stress at R2 is typically much smaller than the surface stress, both in similar storm events and in the rapidly shifting surface conditions of a tropical storm (Gargett and Savidge 2020, their Figs. 12c and 12b, respectively).

Discounting item 1 above, items 2–4 are potential contributors to observed differences between scatter and/or wind/wave scaling at LEO and R2.

First, I consider the larger scatter observed in the R2 data relative to LEO, and suggest that this results primarily from the stronger tides at R2 (item 2 above). Since the wind/wave scale velocity w_S is considered predictive of pure LC, disruption of pure cells by the effects of clockwise tidal turning with time would produce effects similar to those associated with inertial turning, leading to the less organized structures characteristic of LT and decreasing correlation between measured variance and that predicted using w_S. Although much of the LES literature treating the effects on LC of crosswind mean flow due to tides report results at steady-state (Martinat et al. 2011; Shrestha et al. 2019), among steady-state results Kukulka et al. (2011) discuss one case of the early time-dependent stages of imposition of a crosswind pressure gradient. Initial LC cell structures first weakened as crosswind flow increased from zero, then after $\sim$6 h, the two-cell structure of the initial computational state transitioned to a single weaker cell. Presumably (although not part of the reported computations) the structure would revert to the original when the crosswind flow

subsequently decreased to zero again as part of the tidal cycle. Such temporal evolution under continuously varying tidal flows would provide a source of scatter in the 2 h observational averages which would be expected to be larger for the larger tidal velocities at R2.

Turning now to the lower overall rmsw associated with wind/wave forcing at the deeper site, i.e., the difference in a_S values between the two sites, a potential explanation may lie in the differences 3 and 4 between the physical settings of LEO and R2, particularly when these two are combined. Gargett et al. (2014) first suggested how differences in wave type and/or bottom stress magnitude could lead to different levels of forcing of Langmuir features in different coastal settings. Storm wind-generated waves at LEO and R2 have roughly the same wavelength (about 90 m; Gargett and Wells 2007; Gargett et al. 2014), but move in water of different depth. If the depth is great enough that the wave is effectively in deep water, Stokes shear near the bottom is very small, whereas the same wave in shallower water will have larger near bottom Stokes shear (a single wave of wavelength 90 m has Stokes shear 2 m above the bottom at LEO that is nearly 6 times that at R2 for the same wave amplitude). In the presence of significant near-bottom Stokes shear, vertical vorticity associated with bottom boundary layer turbulence will be rotated into the horizontal, essentially duplicating the CL2 vortex force that is operative near the surface. Thus, waves of intermediate type, i.e., those with significant Stokes shear near the bottom, have two sources of energy forcing Langmuir circulations, rather than the single near-surface source characteristic of deepwater waves. Larger storm-driven bottom stress at LEO will contribute to this additional source by increasing the supply of boundary layer vorticity available for rotation by Stokes shear. Gargett and Savidge (2020, their Fig. 13) demonstrate that LEO indeed has near-bottom LC growth rates (defined in analogy with the surface growth rate g_*) that are much larger than values at R2.

In summary, consider first the effectively deepwater wave case of R2, where the fits shown in Table 2 and Fig. 5 indicate that scaling with the convective scale velocity w_* and *any one* of three suggested forms for a wind/wave scale velocity w_S produces the same value for a_C, within its error bounds. Constancy of a_C reaffirms that the convective scale velocity determined in the atmospheric boundary layer is equally applicable to convection in the OSL, as found in other observational results from situations dominated by convection (Steffen and D'Asaro 2002) or strongly influenced by convection (Lombardo and Gregg 1989).

Fits using u_* and the two suggested forms of w_S calculated with $U_S = \mathrm{int}U_{S3}$ all provide 1/1 relationships between observed and predicted values of rmsw. As mentioned previously, similar linearity using any of the three wind/wave scale velocities (albeit with different values of a_S) would result if $U_S \propto u_*$, i.e., if the Stokes velocity were at least approximately linearly proportional to u_*. The degree to which such a linear relationship is achieved by the R2 data is shown in Fig. 7a. While the linear fit lies (just) within the error bars of the data, the second-order fit is clearly preferable. It is this inaccuracy in the assumption of $U_S \propto u_*$ which leads to the decreased

accuracy (i.e., higher rmse and lower R^2) of the fit using only u_*, relative to those incorporating the slightly nonlinear relationship seen in Fig. 7a. Note, however, that while the fit using u_* has the lowest R^2 of the three considered at R2, even this fit provides $R^2 > 0.8$, not insignificant predictive skill. This result is in general agreement with early analysis of rmsw from neutrally buoyant floats at a deepwater site (D'Asaro 2001).

Use of the surface-layer value in the R2 computations results in a fit that, while linear, is not a line through zero with slope of 1, leading to clear underestimate of large values of observed rmsw (Fig. 5d). This result supports use of a near-surface-integral value of Stokes velocity, computed as an integral over a fixed distance from the surface, rather than a surface-layer value that varies with mixed layer depth, in calculation of wind/wave scaling velocity.

I now return to the anomalous nature of coefficients found for the fit made using $w_{S1} = u_*$ at LEO, where the value obtained for a_C is significantly different from all of the other fits, including LEO fits made using either w_{S2} and w_{S3}, both of which yield values of a_C that agree within error bounds with all of those from R2. The root of this single anomalous fit appears to lie with a different relationship between u_* and U_S at LEO, as seen in Fig. 7b. The second-order fit to the R2 data provides a reasonable fit to the LEO data at low values of u_*: however, the two data points at the highest values of u_* lie clearly above the R2 curve. A possible interpretation of this observation is that the relationship between u_* and U_S depends on whether the waves at LEO are effectively deepwater waves (waves short compared to water depth at low wind forcing) like all observations at R2, or intermediate waves, as documented at higher LEO wind speeds by Gargett et al. (2014). The anomalous fit found at LEO when using u_* alone would then presumably be associated with absence of a continuous quasi-linear relationship (such as that shown in Fig. 7a for R2) between u_* and U_S over the entire range of u_*. While this conclusion is tentative, depending as it does on only two binned data points in the present LEO dataset, it suggests that measurement of the wave field, hence observational determination of U_S, is more important in shallow coastal environments, where wave character can change during a wind event, than it is in locations where surface waves retain deepwater character throughout such an event.

Leaving aside only this case (i.e., the fit at LEO using $w_{S1} = u_*$), the analysis presented here enables prediction of rmsw, the root-mean-square vertical velocity fluctuation associated with turbulence generated by a mixture of forcing by wind/wave processes and convection at both shallow and deep coastal sites, within reported errors associated with determination of the coefficients in Eq. (1). The predictor is a linear combination of scale velocities appropriate for convective and wind/wave (Langmuir) turbulence. The coefficient of the convective scale velocity a_C is constant, within error bounds, independent of the form chosen for the wind/wave scale velocity, affirming the assumption that the two forcings are independent, hence that their results can be combined linearly. The value of $a_C \sim 0.5$ lies within the range of values found by other observations. The coefficient of the wind/wave scale velocity a_S depends on the form used for w_S. In both locations,

overall goodness-of-fit parameters (rmse and R^2) are nearly identical for fits using w_{S2} and w_{S3} calculated with $U_S = \text{int}U_{S3}$, hence the present analysis provides no guidance as to which should be preferred as a wind/wave scale velocity. However, it does indicate that in calculating such scale velocities, a near-surface-integral value of the Stokes velocity is preferable to a surface-layer value, i.e., neither removal of a deep reference value nor use of a mean over a depth that depends on mixed layer depth H is supported by the present data.

Both LEO and R2 datasets inevitably include situations with directional spread of the wave spectrum about the wind direction, wind–wave directional misalignment, as well as a range of wave ages. The linearity of the predictions, plus the tightness of the results at LEO, where tidal effects should be minimal, indicate that none of these factors produce effects large enough to preclude a useful prediction of rmsw based solely on surface forcing fields.

Finally, given the deepwater character of even storm waves at R2, plus bottom stress that is much smaller than the applied surface stress, it is tempting to conclude that the scalings provided here from analysis of the R2 data can be used in truly deep water sites, i.e., where the bottom of the OSL is a pycnocline rather than a solid surface. However, a reviewer of this manuscript suggested that such a conclusion is unwarranted because the coefficient of $a_S \sim 0.7$ obtained for the R2 fit using the scale velocity $w_{S1} = u_*$ is smaller than both values obtained for boundary layer turbulence not impacted by waves and values estimated from open ocean measurements by (nearly) neutrally buoyant floats (D'Asaro 2001; D'Asaro et al. 2014), the only other source of direct information about oceanic rmsw. It is actually reasonable that turbulence in a wavy boundary layer should be weaker than that in an ocean boundary layer without waves (should such exist in the real world), since part of the stress applied to the surface in the former case goes into generation of surface waves, rather than to mean currents and their associated BL turbulence. Turning to the floats, while they certainly provide striking confirmation of motion in the turbulent large eddies of the OSL, it seems possible that quantitative results reported from the float data may be biased high. The slight positive buoyancy of a float causes a number of known effects by which the floats overestimate rmsw. When corrected for a number of these effects, the original float results of D'Asaro (2001; data reportedly unaffected by surface buoyancy flux) led to a value of $a_S \sim 1$ in a relationship rmsw $= a_S u_*$.[3] However, no correction was made for the fact that the upward buoyancy of the floats causes them to oversample the more energetic downward-going plumes leaving the surface. While D'Asaro (2001) dismissed this by remarking that the effect is likely small, it nonetheless follows that $a_S \sim 1$ is an upper bound for these measurements. In a larger deep ocean dataset (D'Asaro et al. 2014) that also finds $a_S \sim 1$, float measurements of wvar are corrected for the effect of surface cooling. By itself, convection drives boundary layer turbulence with wvar$_* = a_C^2 w_*^2$ where a_C is

in the range (Steffen and D'Asaro 2002) of 0.3–0.5. D'Asaro et al. (2014) thus corrected observed wvar for buoyancy effects by forming wvar$^{\text{neutral}}$ = wvar − wvar$_*$, where wvar$_*$ was calculated using $a_C^2 = 0.3$. However, an outstanding question is whether it is the velocity *variances* of the two contributing processes that add, as assumed in the above correction, or the velocities themselves, as seems more physically reasonable and as is posited here. In this latter case,

$$\text{wvar} = (a_C w_* + a_S u_*)^2 = a_S^2 u_*^2 + (a_C^2 w_*^2 + 2a_C a_S w_* u_*),$$

hence

$$a_S^2 u_*^2 = (\text{wvar} - \text{wvar}_*) - 2a_C a_S w_* u_*,$$

i.e., the observed total variance wvar should have a correction in addition to wvar$_*$, further reducing the value computed for a_S from the float measurements of wvar (unfortunately the unknown a_S appears in the additional correction, but could presumably be determined by an iterative scheme). Given these uncertainties in corrections for float behaviors and for surface buoyancy forcing, all contributing to *over*estimation of wvar in the float datasets, it seems possible that the value of $a_S \sim 0.7$ obtained here is not after all incompatible with the float measurements. It is nevertheless clearly desirable to obtain observations comparable to those presented here from a true deep ocean surface boundary layer, in order to confirm the present suggestion that the R2 coefficients are applicable to the deep water case, as well as the previous conclusion that a near-surface-integral value of the Stokes velocity is preferable to a surface-layer value. While standard observational procedures are available for measuring the necessary wind/wave forcing fields in the deep ocean environment, the outstanding challenge, as discussed in G22, is to provide power and bandwidth sufficient to obtain time-continuous information on large-scale turbulent structure and intensity, similar to that analyzed here, in a truly deep water location. Mounting an appropriate (narrow vertical beam beamwidth) VADCP looking upward from a gimballed enclosure on a stiff subsurface mooring and cabling to an oil rig in water deep enough that the surface mixed layer remains well above the bottom would enable such measurements. Such a deployment is strongly encouraged.

The observational analysis of Belcher et al. (2012) and the present results both strongly suggest that relevant models of OSL turbulence must treat a realistic combination of both wind/wave effects and convection (either nocturnal or quasi-continuous over longer storm periods). However, an assumption inherent to the present analysis is that OSL turbulence adapts reasonably rapidly to changes in surface forcing, hence turbulence characteristics averaged over a 2-h time period can be characterized by surface forcing averaged over that same time period. Observations reported in G22 suggest that this is true for changes in wind/wave forcing, but that the adjustment time for changes in buoyancy flux may be somewhat longer. Although beyond the scope of the present investigation, determination of time scales of buoyancy response in situations of mixed forcings will be particularly important for applications

---

[3] For clarity, this discussion uses the notation of the present paper, rather than that of the original publication(s).

such as the plankton/particulate distributions mentioned in section 1.

APPENDIX

Correction of intU_{S3} for Missing High-Frequency Variance

The total Stokes velocity is larger than the measured part $U_S^M(x_3)$ by the amount of variance between ω_M and the Forristall (1981) wave breaking frequency $\omega_B = 0.0061g/u_*$ (Clarke and Van Gorder 2018),

$$U_S(x_3) = U_S^M(x_3) + \frac{2}{g}\int_{\omega_M}^{\omega_B} S(\omega)\omega^3\exp[2(\omega^2/g)x_3]d\omega, \quad \text{(A1)}$$

where the second correction term uses the deepwater form of the Stokes velocity integral [GG14, their Eq. (A5)] since the missing variance is due to high frequency, hence deepwater waves.

The Toba (1973) spectral form

$$S(\omega) = \alpha_{\text{Toba}}gu_*\left(\frac{\rho_w}{\rho_{\text{air}}}\right)^{1/2}\omega^{-4}, \text{ with } \alpha_{\text{Toba}} = 0.11$$

(see appendix of G22), describes the spectral shape above the spectral peak of $\phi_\zeta(\omega)$, hence the resulting corrected spectrum is

$$U_S(x_3) = U_S^M(x_3) + A_{\text{Toba}}\int_{\omega_M}^{\omega_B}\omega^{-1}\exp[2(\omega^2/g)x_3]d\omega,$$

$$\text{where } A_{\text{Toba}} \equiv 2\alpha_{\text{Toba}}u_*\left(\frac{\rho_w}{\rho_{\text{air}}}\right)^{1/2}. \quad \text{(A2)}$$

Integrating Eq. (A2) from $x_3 = -h = -3$ m to 0 gives

$$\text{int}U_{S3} = \text{int}U_{S3}^M + \frac{1}{h}\left\{\int_{-3}^0\left[A_{\text{Toba}}\int_{\omega_M}^{\omega_B}\omega^{-1}\exp(2\omega^2x_3/g)d\omega\right]dx_3\right\},$$

where $\text{int}U_{S3}^M = (1/h)\int_{-3}^0 U_S^M(x_3)dx_3$ is the directly measured part of the variable.

The correction term is derived by first carrying out the vertical integral:

$$\int_{-3}^0 \exp(2\omega^2x_3/g)dx_3 = \frac{g}{2\omega^2}\exp(2\omega^2x_3/g)|_{-3}^0$$

$$= \frac{g}{2\omega^2}[1 - \exp(-6\omega^2/g)] \approx \frac{g}{2\omega^2},$$

where the simplification is justified within a few percent when using $h = 3$ m because at the lowest frequency (ω_M) that will be involved in the frequency integral, hence the largest value of $\exp(-6\omega^2/g)$, the second term in brackets is, only ~0.022 ≪ 1. With the above simplification, the correction term becomes

$$\frac{A_{\text{Toba}}}{h}\int_{\omega_M}^{\omega_B}\omega^{-1}\frac{g}{2\omega^2}d\omega = \frac{A_{\text{Toba}}g}{2h}\int_{\omega_M}^{\omega_B}\omega^{-3}d\omega$$

$$= \frac{-A_{\text{Toba}}g}{4h}\int_{\omega_M}^{\omega_B}d(\omega^{-2})d\omega$$

$$= \frac{A_{\text{Toba}}g}{4h}(\omega_M^{-2} - \omega_B^{-2}) > 0,$$

hence the corrected value is

$$\text{int}U_{S3} = \text{int}U_{S3}^M + \frac{A_{\text{Toba}}g}{4h}(\omega_M^{-2} - \omega_B^{-2}). \quad \text{(A3)}$$

Note that the correction is a function only of u_*, which enters both A_{Toba} and ω_B, and goes to zero both as $u_* \to 0$ and as $u_* \to 0.024$ m s^{-1}, the value at which $\omega_B \to \omega_M$ (from above) and beyond which no correction for missing variance is necessary. The maximum correction (~0.007 m s^{-1} at $u_* \sim 0.015$ m s^{-1}) is ~10% of the values of $\text{int}U_{S3}^M \sim 0.06$–0.07 m s^{-1} typical of LSC.

REFERENCES

Belcher, S. E., and Coauthors, 2012: A global perspective on Langmuir turbulence in the ocean surface boundary layer. *Geophys. Res. Lett.*, **39**, L18605, https://doi.org/10.1029/2012GL052932.

Bidlot, J.-F., 2020: IFS Documentation CY47R1 - Part VII: ECMWF wave model. ECMWF Tech. Memo. 7, 114 pp., https://doi.org/10.21957/31drbygag.

Clarke, A. J., and S. Van Gorder, 2018: The relationship of near-surface flow, Stokes drift and the wind stress. *J. Geophys. Res. Oceans*, **123**, 4680–4692, https://doi.org/10.1029/2018JC014102.

Csanady, G. T., 1994: Vortex pair model of Langmuir circulation. *J. Mar. Res.*, **52**, 559–581.

D'Asaro, E. A., 2001: Turbulent vertical kinetic energy in the ocean mixed layer. *J. Phys. Oceanogr.*, **31**, 3530–3537, https://doi.org/10.1175/1520-0485(2002)031<3530:TVKEIT>2.0.CO;2.

——, J. Thomson, A. Y. Shcherbina, R. R. Harcourt, M. F. Cronin, M. A. Hemer, and B. Fox-Kemper, 2014: Quantifying upper ocean turbulence driven by surface waves. *Geophys. Res. Lett.*, **41**, 102–107, https://doi.org/10.1002/2013GL058193.

Fan, Y. Y., and Coauthors, 2020: The effect of Langmuir turbulence under complex real oceanic and meteorological forcing. *Ocean Modell.*, **149**, 101601, https://doi.org/10.1016/j.ocemod.2020.101601.

Forristall, G. Z., 1981: Measurements of a saturated range in ocean wave spectra. *J. Geophys. Res.*, **86**, 8075–8084, https://doi.org/10.1029/JC086iC09p08075.

Gargett, A. E., 2022: Forcing space: An alternative to regime diagrams for predicting characteristics of turbulence in the ocean surface mixing layer. *J. Phys. Oceanogr.*, **52**, 519–535, https://doi.org/10.1175/JPO-D-21-0145.1.

——, and J. R. Wells, 2007: Langmuir turbulence in shallow water: Part I. Observations. *J. Fluid Mech.*, **576**, 27–61, https://doi.org/10.1017/S0022112006004575.

——, and C. E. Grosch, 2014: Turbulence process domination under the combined forcings of wind stress, the Langmuir vortex force, and surface cooling. *J. Phys. Oceanogr.*, **44**, 44–67, https://doi.org/10.1175/JPO-D-13-021.1.

——, and D. J. Savidge, 2020: Winds, waves and turbulence on a shallow continental shelf during passage of a tropical storm. *J. Phys. Oceanogr.*, **50**, 1341–134, https://doi.org/10.1175/JPO-D-20-0024.1.

——, D. K. Savidge, and J. R. Wells, 2014: Anatomy of a Langmuir supercell event. *J. Mar. Res.*, **72**, 127–163, https://doi.org/10.1357/002224014814901976.

Grant, A. L. G., and S. E. Belcher, 2009: Characteristics of Langmuir turbulence in the ocean mixed layer. *J. Phys. Oceanogr.*, **39**, 1871–1887, https://doi.org/10.1175/2009JPO4119.1.

Grosch, C. E., and A. E. Gargett, 2016: Why do LES of Langmuir supercells not include rotation? *J. Phys. Oceanogr.*, **46**, 3595–3597, https://doi.org/10.1175/JPO-D-16-0092.1.

Harcourt, R. R., and E. A. D'Asaro, 2008: Large-eddy simulation of Langmuir turbulence in pure wind seas. *J. Phys. Oceanogr.*, **38**, 1542–1562, https://doi.org/10.1175/2007JPO3842.1.

Holtslag, A. A. M., and F. T. M. Nieuwstadt, 1986: Scaling the atmospheric boundary layer. *Bound.-Layer Meteor.*, **36**, 201–209, https://doi.org/10.1007/BF00117468.

Kenyon, K. E., 1969: Stokes drift for random gravity waves. *J. Geophys. Res.*, **74**, 6991–6994, https://doi.org/10.1029/JC074i028p06991.

Kukulka, T., and R. R. Harcourt, 2017: Influence of Stokes drift decay scale on Langmuir turbulence. *J. Phys. Oceanogr.*, **47**, 1637–1656, https://doi.org/10.1175/JPO-D-16-0244.1.

——, A. J. Plueddemann, J. H. Trowbridge, and P. P. Sullivan, 2009: Significance of Langmuir circulation in upper ocean mixing: Comparison of observations and simulations. *Geophys. Res. Lett.*, **36**, L10603, https://doi.org/10.1029/2009GL037620.

——, ——, ——, and ——, 2011: The influence of crosswind tidal currents on Langmuir circulation in a shallow ocean. *J. Geophys. Res.*, **116**, C08005, https://doi.org/10.1029/2011JC006971.

Leibovich, S., 1977: Convective instability of stably stratified water in the ocean. *J. Fluid Mech.*, **82**, 561–581, https://doi.org/10.1017/S0022112077000846.

——, 1983: The form and dynamics of Langmuir circulations. *Annu. Rev. Fluid Mech.*, **15**, 391–427, https://doi.org/10.1146/annurev.fl.15.010183.002135.

Li, M., L. Sanford, and S.-Y. Chao, 2004: Effects of time dependence in unstratified tidal boundary layers: Results from large eddy simulations. *Estuarine Coastal Shelf Sci.*, **65**, 193–204, https://doi.org/10.1016/j.ecss.2004.08.017.

Li, S., M. Li, G. P. Gerbi, and J.-B. Song, 2013: Roles of breaking waves and Langmuir circulation in the surface boundary layer of a coastal ocean. *J. Geophys. Res.*, **118**, 5173–5187, https://doi.org/10.1002/jgrc.20387.

Lombardo, C. P., and M. C. Gregg, 1989: Similarity scaling of viscous and thermal dissipation in a convecting surface boundary layer. *J. Geophys. Res.*, **94**, 6273–6284, https://doi.org/10.1029/JC094iC05p06273.

Martinat, G., Y. Xu, C. E. Grosch, and A. E. Tejada-Martinez, 2011: LES of turbulent surface shear stress and pressure-gradient-driven flow on shallow continental shelves. *Ocean Dyn.*, **61**, 1369–1390, https://doi.org/10.1007/s10236-011-0450-3.

McWilliams, J. C., P. P. Sullivan, and C.-H. Moeng, 1997: Langmuir turbulence in the ocean. *J. Fluid Mech.*, **334**, 1–30, https://doi.org/10.1017/S0022112096004375.

Noh, Y., H. S. Min, and S. Raasch, 2004: Large eddy simulation of the ocean mixed layer: The effects of wave breaking and Langmuir circulation. *J. Phys. Oceanogr.*, **34**, 720–735, https://doi.org/10.1175/1520-0485(2004)034<0720:LESOTO>2.0.CO;2.

Plueddemann, A. J., J. A. Smith, D. M. Farmer, R. A. Weller, W. R. Crawford, R. Pinkel, S. Vagle, and A. Gnanadesikan, 1996: Structure and variability of Langmuir circulation during the surface waves processes program. *J. Geophys. Res.*, **101**, 3525–3543, https://doi.org/10.1029/95JC03282.

Polton, J. A., and S. E. Belcher, 2007: Langmuir turbulence and deeply penetrating jets in an unstratified mixed layer. *J. Geophys. Res.*, **112**, C09020, https://doi.org/10.1029/2007JC004205.

Savidge, D. K., and A. E. Gargett, 2017: Langmuir supercells on the middle shelf of the South Atlantic Bight: 1. Cell structure. *J. Mar. Res.*, **75**, 49–79.

Shrestha, K., W. Anderson, A. Tejada-Martinez, and J. Kuehl, 2019: Orientation of coastal-zone Langmuir cells forced by wind, wave and mean current at variable obliquity. *J. Fluid Mech.*, **879**, 716–743, https://doi.org/10.1017/jfm.2019.683.

Skyllingstad, E. D., and D. W. Denbo, 1995: An ocean large-eddy simulation of Langmuir circulations and convection in the surface mixed layer. *J. Geophys. Res.*, **100**, 8501–8522, https://doi.org/10.1029/94JC03202.

Smith, J. A., 1996: Observations of Langmuir circulation, waves, and the mixed layer. *The Air-Sea Interface: Radio and Acoustic Sensing, Turbulence, and Wave Dynamics*, M. A. Donelan, W. H. Hui, and W. J. Plant, Eds., University of Toronto Press, 613–622.

Steffen, E. L., and E. A. D'Asaro, 2002: Deep convection in the Labrador Sea as observed by Lagrangian floats. *J. Phys. Oceanogr.*, **32**, 475–492, https://doi.org/10.1175/1520-0485(2002)032<0475:DCITLS>2.0.CO;2.

Sullivan, P. P., J. C. McWilliams, and W. K. Melville, 2004: The oceanic boundary layer driven by wave breaking with stochastic variability. Part 1. Direct numerical simulations. *J. Fluid Mech.*, **507**, 143–174, https://doi.org/10.1017/S0022112004008882.

——, ——, and ——, 2007: Surface gravity wave effects in the oceanic boundary layer: Large-eddy simulation with vortex force and stochastic breakers. *J. Fluid Mech.*, **593**, 405–452, https://doi.org/10.1017/S002211200700897X.

——, L. Romero, J. C. McWilliams, and W. K. Melville, 2012: Transient evolution of Langmuir turbulence in ocean boundary layers driven by hurricane winds and waves. *J. Phys. Oceanogr.*, **42**, 1959–1980, https://doi.org/10.1175/JPO-D-12-025.1.

Teixeira, M. A. C., and S. E. Belcher, 2002: On the distortion of turbulence by a progressive surface wave. *J. Fluid Mech.*, **458**, 229–267, https://doi.org/10.1017/S0022112002007838.

Tejada-Martínez, A. E., and C. E. Grosch, 2007: Langmuir turbulence in shallow water: Part II. Large-eddy simulation. *J. Fluid Mech.*, **576**, 63–108, https://doi.org/10.1017/S0022112006004587.

Toba, Y., 1973: Local balance in the air-sea boundary process. *J. Oceanogr. Soc. Japan*, **29**, 209–220, https://doi.org/10.1007/BF02108528.

Tseng, R.-S., and E. A. D'Asaro, 2004: Measurements of turbulent vertical kinetic energy in the ocean mixed layer from Lagrangian floats. *J. Phys. Oceanogr.*, **34**, 1984–1990, https://doi.org/10.1175/1520-0485(2004)034<1984:MOTVKE>2.0.CO;2.

Van Roekel, L. P., B. Fox-Kemper, P. P. Sullivan, P. E. Hamlington, and S. R. Haney, 2012: The form and orientation of Langmuir cells for misaligned winds and waves. *J. Geophys. Res.*, **117**, C05001, https://doi.org/10.1029/2011JC 007516.

Walker, R., A. E. Tejada-Martínez, and C. E. Grosch, 2016: Large-eddy simulation of a coastal ocean under the combined effect of surface heat fluxes and full-depth Langmuir circulation. *J. Phys. Oceanogr.*, **46**, 2411–2436, https://doi.org/10. 1175/JPO-D-15-0168.1.

Wang, X., and T. Kukulka, 2021: Ocean surface boundary layer response to abruptly turning winds. *J. Phys. Oceanogr.*, **51**, 1779–1794, https://doi.org/10.1175/JPO-D-20-0198.1.

——, ——, and A. J. Plueddemann, 2022: Wind fetch and direction effects on Langmuir turbulence in a coastal ocean. *J. Geophys. Res. Oceans*, **127**, e2021JC018222, https://doi.org/10. 1029/2021JC018222.

Yan, C., J. C. McWilliams, and M. Chamecki, 2022: Overlapping boundary layers in coastal oceans. *J. Phys. Oceanogr.*, **52**, 627–646, https://doi.org/10.1175/JPO-D-21-0067.1.